The Character and Changing Frequency of Extreme California Fire Weather

Andreas Franz Prein[1], Janice L. Coen[1], and Abigail Jaye[1]

[1]National Center for Atmospheric Research (UCAR)

November 23, 2022

Abstract

Five of California's ten largest wildfires occurred in 2020, with the largest complex shattering the previous record by more than 100 %. The year follows a decade containing extraordinary fire activity. Trend investigations focused on changes in human activities and atmospheric thermodynamics, while the impacts of changing atmospheric dynamics are largely unknown. Here we identify extreme weather types (XWTs) associated with historically large daily burned areas in eight Californian regions. These XWTs characterize dominant fire weather regimes varying in fire behavior types (plume-driven vs. wind-driven fires) and seasonality. 2020's exceptional fires partly occurred during previously unrecognized XWTs, whose characteristics and recurrence intervals were largely unknown. Most of the strongly large-scale forced XWTs such as Santa Ana and Diablo events increased in frequency during the 20th century particularly in the Sand Diego and Bay Area region. These changes are likely not anthropogenically caused and predominantly due to climate internal variability. However, raising greenhouse gas concentrations significantly decrease thermal low XWTs in southern and increase them in central California. These XWTs occur during the hottest time in the year and will alter fire risk in the summer season.

The Character and Changing Frequency of Extreme California Fire Weather

Andreas F Prein[1*], and Janice Coen[1,2], and Abby Jaye[1]

[1]National Center for Atmospheric Research (NCAR), Boulder, CO, USA
[2]University of San Francisco, San Francisco, CA, USA

Key Points:

- We identify archetypal extreme fire weather types (XWTs) in eight Californian regions.
- 20th century XWT frequency changes are primary caused by natural climate variability.
- Raising GHG concentrations increase heat-low XWTs in central California and decrease them in the south.

*3090 Center Green Dr., Boulder, CO 80301, USA

Corresponding author: Andreas F. Prein, `prein@ucar.edu`

Abstract

Five of California's ten largest wildfires occurred in 2020, with the largest complex shattering the previous record by more than 100%. The year follows a decade containing extraordinary fire activity. Trend investigations focused on changes in human activities and atmospheric thermodynamics, while the impacts of changing atmospheric dynamics are largely unknown. Here we identify extreme weather types (XWTs) associated with historically large daily burned areas in eight Californian regions. These XWTs characterize dominant fire weather regimes varying in fire behavior types (plume-driven vs. wind-driven fires) and seasonality. 2020's exceptional fires partly occurred during previously unrecognized XWTs, whose characteristics and recurrence intervals were largely unknown. Most of the strongly large-scale forced XWTs such as Santa Ana and Diablo events increased in frequency during the 20th century particularly in the Sand Diego and Bay Area region. These changes are likely not anthropogenically caused and predominantly due to climate internal variability. However, raising greenhouse gas concentrations significantly decrease thermal low XWTs in southern and increase them in central California. These XWTs occur during the hottest time in the year and will alter fire risk in the summer season.

1 Introduction

In the U.S., California is the state with the highest exposure to wildfires with approximately 2,019,800 properties at risk (Verisk, 2020). The combination of increasing annually burned area (Westerling, 2016; Abatzoglou & Williams, 2016) and large exposure resulted in exceptional economic losses with more than 20US$ bn in 2018 alone (Re, 2019). Potential causes for the large increase in burned area in California (FIRE, 2020) are manifold (Jin et al., 2014) and include an increase in atmospheric temperature and aridity caused by climate variability and change (Abatzoglou & Williams, 2016; Williams et al., 2019), a decrease of precipitation in recent decades due to fewer winter storms(Prein et al., 2016), an earlier start and later end of the fire season (Jolly et al., 2015), changes in forest management (Parks et al., 2015; Tempel et al., 2014), an increase in population (Radeloff et al., 2018), and its expansion of dwellings and infrastructure into former wildlands (Hammer et al., 2007). Since the early 2000s, sub-daily moderate resolution satellite active fire detection observations have enabled products that estimate daily burned area on local scales (Artés et al., 2019; Davies et al., 2019), revolutionizing our ability to detect fire occurrence and progression. These observations show that the annual total burned area in California is disproportionately affected by a few large fires and those fires themselves burn most of the total burned area on only a few days.

Traditionally, fire weather indexes (e.g. Red Flag Warning (Clark et al., 2020), Fosberg Fire Weather Index (Fosberg, 1978; Goodrick, 2002), the Hot/Dry/Windy Index (Srock et al., 2018)) are used to predict days with the potential for rapid fire spread. Those indices typically depend on local observations that account for atmospheric static stability and humidity profile in the lower atmosphere (Haines, 1989), fuel condition (Amiro et al., 2005), and low-level wind speed (Amiro et al., 2005). More recent studies also found that upper-level and nocturnal meteorology can lead to rapid-fire-spread (Peterson et al., 2015).

Here, we focus on the large-scale atmospheric conditions that were present during days of large daily fire growth in California's recent history. We hypothesise that there is a limited set of extreme weather types (XWTs) that favor large daily fire growth, which builds of research from the 1960s (Hull et al., 1966). Some of these patterns are well known such as strong ridging east of California that causes Santa Ana (Raphael, 2003) and Diablo wind events (Smith et al., 2018). However, there are many examples of extreme daily burned areas across California that happened under different or much weaker large-scale forcing. Here, we exploit multiple daily burned area observations, state-of-the-art atmospheric reanalyses datasets, and earth system modeling results to classify XWTs in eight California fire regions and attribute XWT frequency changes throughout the 20th and 21st century to natural climate variability, increasing greenhouse-gas concentrations, and changes in aerosol forcing.

2 Data and Methods

2.1 Fire Observations and Fire Regions

We use several observational datasets to analyze the characteristics of extreme fires in California. The longest record that we use is the Monitoring Trends in Burn Severity (MTBS) (Eidenshink et al., 2007) dataset, which contains total (final) burned area estimates for 1,630 fires in California within the period 1984–2016 (Fig. 1a). Most of these fires were small with a median burned area of $\sim$10 km^2 (MTBS record's fires larger than $\sim$4 km^2). However, the fire area size distribution has a very long tail with the top three fires having each burned an area larger than 1,000 km^2 (roughly half the size of Rhode Island). We use MTBS only for comparison with daily burned area products and to understand the representatives of fires in the 21st century compared to longer records.

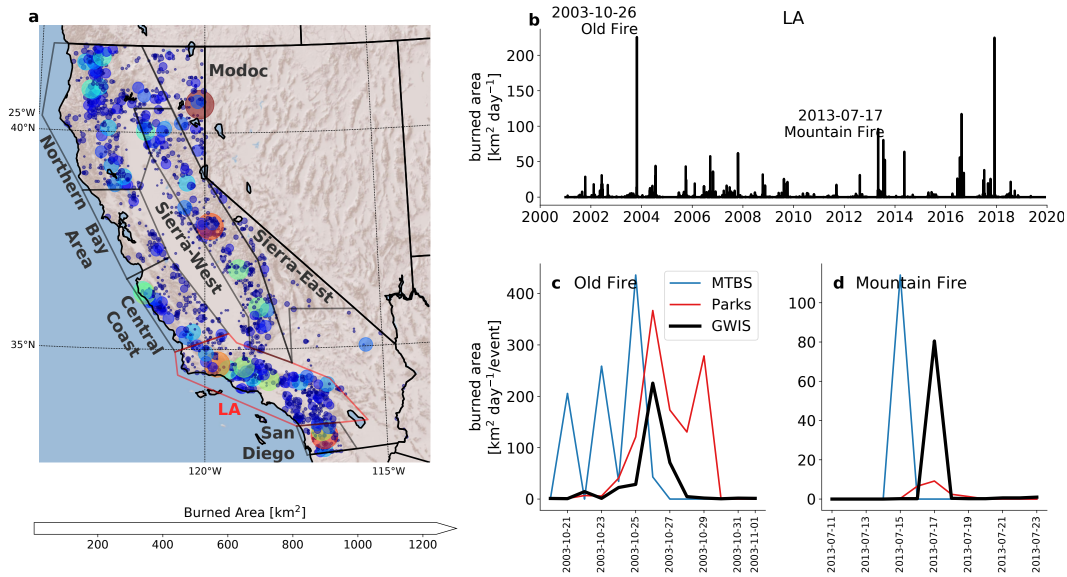

Figure 1. California fire regions and accumulated burned area (indicated by dot size and color) of fires from the MTBS dataset covering 1984 to 2016 (a). The accumulated daily burned area time series for the LA region (highlighted in red outline in (a)) based on the GWIS dataset is shown in (b). A closer look at the daily evolution of the Old Fire and Mountain Fire is shown in (c) and (d), respectively, based on the MTBS (blue), Parks (red), and GWIS (black) data. Note that MTBS contains only the total burned area for each fire recorded at the extinction date of the fire rather than a daily burned area.

To understand how these extreme fires evolve temporally, we employed daily burned area estimates based on satellite active fire detection data collected since 2000. These products area estimates are primarily based on satellite observations that are subject to considerable uncertainties (Thompson & Calkin, 2011) (Fig. 1c,d). In this study, we are interested in evaluating the large-scale atmospheric conditions on days with extreme burned areas. Uncertainties in the absolute amount of burned area do not affect our analysis as long as the same days are identified as extreme. The here used observational burned-area datasets vary in their spatiotemporal resolution, the covered period, and input data. Besides MTBS, we use two daily burned area products that are based on the MODIS (Moderate Resolution Imaging Spectroradiometer) burned area product Collection 6 (MCD64A1) (Giglio et al., 2018). The first is the Global Wildfire Information System (GWIS) dataset (Artés et al., 2019) that has global coverage between January 2001 to November 2019 and the second is provided by Sean Parks (Parks, 2014) and covers 2002–2018. We decided to use the GWIS dataset to perform our analysis due to its longer period and improved skill in defining XWTs (not shown).

For the analysis of 2020 fires, we use the near-real-time (NRT) and standard quality thermal anomaly (archived) datasets from NASA's Fire Information for Resource Management System (FIRMS) (Davies et al., 2019) based on MODIS NRT/archived (MCD14DL/MCD14ML) and VIIRS 375 m NRT/archived (VNP14IMGTDL/VNP14IMGTML) observations. The archived (quality controlled) datasets replace the NRT datasets with a 3-month lag. Both datasets report pixels in which fires were detected each day, which does not directly translate to the burned area since pixels are also reported if only a fraction of their area was burned.

The analysis is performed on eight "homogeneous" fire regions that feature similar fuel and fire weather conditions (Fig. 1a). These regions are similar to the regions defined in California's Fourth Climate Change Assessment (Bedsworth et al., 2018) except that we have split the Sierra Nevada region into east and west parts to account for their different fire weather conditions. No XWTs were derived for the Central Valley and the Desert Southwest due to their small sample size of observed fires. The Northern and Sierra regions are mainly forested while the central and southern coastal regions feature chaparral, grass-oak savanna, and urban areas. Also, fire ignition varies between regions and is mostly human-caused in urbanized regions, caused by dry lightning in the Northern and Modoc regions, and of mixed natural and human-caused ignitions in the Sierra regions (Balch et al., 2017).

2.2 Atmospheric Variables

The XWT analysis was performed by using daily average (daily minimum and maximum for 2 m temperature) atmospheric fields from the European Centre for Medium-Range Weather Forecasts' (ECMWF) fifth generation global reanalysis (ERA5) (Hersbach et al., 2020) over the GWIS data record. ERA5 assimilates a large variety of observational data including satellite, surface-based, and airborne data. We tested 33 variables concerning their predictability for extreme daily burned areas, which can be separated in dynamical forcing (zonal, meridional, and total wind speed at 10 m, 850 hPa, 500 hPa, and 200 hPa; geopotential height at 500 hPa; sea level pressure), thermodynamic forcing (air temperature at 2 m, 850 hPa, and 500 hPa), moisture (mixing ratio, relative humidity, and moisture flux at 2 m, 850 hPa, and 500 hPa and precipitable water), and convective forcing (convective available potential energy, convective inhibition, level of free convection, and lifting condensation level). These variables were selected due to their relevance in prescribing the large-scale flow conditions and their impact on fire behavior.

To analyse historic and projected future changes in XWT frequencies in each of the eight California fire regions we detect XWT days in in three ensemble datasets.

First, we use the third version of the NOAA-CIRES-DOE 20th Century Reanalysis (NCD20C) (Slivinski et al., 2019) to understand historic changes in XWT frequencies. NCD20C is a probabilistic reanalysis product with 80 ensemble members that allow the statistical analysis of XWT trends within the period 1900–2015. It has an effective resolution of 60 km at the equator, assimilates a large set of pressure observations, and is forced by pre-described sea surface temperature and sea ice fields. It has a largely improved representation of storm intensity, more accurate estimates of confidence intervals, reduced errors, and large-scale reductions in model biases than previous versions.

Second, we analyze the Community Earth System Model (CESM) large ensemble dataset (LENS) (Kay et al., 2015) to understand the impact of natural variability and forced climate change on XWT frequencies. LENS consists of 40 ensemble members that are identical except for chaotic perturbation of the initial condition temperatures. The model grid spacing is one degree and each member covers the period 1920–2100. Historic forcing are applied to the period 1920-2005 and representative concentration pathway 8.5 (RCP8.5) forcing were used from 2006–2100 (Meinshausen et al. 2011; Lamarque et al. 2011).

The third dataset that we use in the XWT frequency change analysis are CESM single forcing experiments (Deser et al., 2020). These simulations are identical to the LENS simulations except for one forcing agent being held constant on its 1920 level. We are using the fixed greenhouse gas (no-GHG) and fixed aerosol (no-AER) ensemble in this study. Each of them consist of 20-members that vary in slight temperature perturbations in 1920 and provide data until 2080. The effect of e.g., greenhouse gases on XWT frequencies is derived from the difference between the single forcing run with constant greenhouse gasses and the full forcing (LENS) simulations.

For assessing the large-scale patterns that were associated with the 2020 fires, we use analysis data from ECMWF's integrative forecasting system (IFS) (Gregory et al., 2000). IFS is the operational forecasting model of ECMWF and analysis data is available in near real-time whereas ERA5 data has a time lag of a few months.

2.3 Extreme Weather Typing (XWT) Analysis

We use the GWIS daily burned area product to define XWTs because of its long period and favorable performance (i.e., higher skill scores) in defining XWTs compared to using the Parks dataset (not shown). First, we accumulate the daily burned area in each of the eight fire regions and select the top N events that are at least 7 days apart. Second, we load the 33 ERA5 variables in a region that is 5° larger than the edges of the sub-region of interest within the GWIS period (Jan. 2001 to Nov 2019). The variables are pre-processed by removing the annual cycle through subtracting the domain average low-pass filtered (21-day equal filter length) time series from each day. Next, we remove the domain average linear trend to minimize the impact of climate change and variability on the XWTing and calculate climatological anomaly fields. In the last preprocessing step, we normalize the daily fields to give the variables equal weight and to constrain the analysis solely to spatial patterns. It is important to mention that the usage of normalized anomaly patterns (i.e. spatial gradients) does not account for variable amounts (e.g., how hot it was on an extreme fire day). This generally improves the XWTing skill and allows us to differentiate between changes in the large-scale dynamics (e.g., the frequency of an extreme pattern) and changes in its thermodynamics (e.g., the temperature on extreme fire days). After the preprocessing, the top N days concerning burned area are selected and the data is clustered by using hierarchical density-based clustering (HDBSCAN) (McInnes et al., 2017). For more details on the XWTing algorithm see Prein and Mearns (Prein & Mearns, 2021).

We optimize the cluster analysis by testing all possible combinations of up to three variables out of the 33 variables (6017 possible combinations). Previous analysis has shown that using three or fewer variables results in close to optimum clustering performance and also substantially reduces the necessary computational costs (Prein & Mearns, 2021). In addition to the variable combination, we also test N (the number of considered extreme events) equal 4, 6, 10, and 15. A summary of this analysis and the selected variable combination that resulted in optimal skill in each sub-region is shown in Fig. S1. The variables that result in the highest predictive skill are mostly related to low-level moisture and temperature patterns. The lifting condensation level pattern is particularly important in the Modoc, Sierra East, Sierra West, and Bay Area (Fig. S1).

The skill of the XWTing is calculated from a split-sample analysis where XWTs are derived based on one half of the data period and their skill is evaluated compared to the other half. XWTs are skillful if they allow identifying extreme fire days based on their similarity (Euclidean distance) to an XWT centroid (mean state) and individual days within each XWT. Several skill scores were tested and we decided to use the average of two scores that target different error characteristics.

The first score is the "area under the ROC (Receiver Operating Characteristics) curve" (AUC) (Wilks, 2011) skill score. The ROC curve is based on two parameters at different classification thresholds – the False Positive Rate (the ratio of false positives to false positives and true negatives) and the True Positive Rate (the ratio of true positive to true positive and false negative). The AUC is the integral under the ROC curve where a value of 1.0 indicates a perfect model and a value of 0.5 indicates a model with no skill.

The second score is the Average Precision-Recall score (Saito & Rehmsmeier, 2015) (APR). Similar to the AUC this score consists of two variables - precision and recall. Precision is defined as the ratio between true positive to true positive plus false positive and recall measures the ratio between true positive to true positive and false negatives. The APR is the integral under the precision-recall curve and varies between 0.0 and 1.0, where 1.0 indicates a perfect model.

In addition to the split-sample testing, we also test the predictive skill of XWTs by removing single years with extreme burned area days from the training period and test if the derived XWTs allow detecting the removed extreme event day according to its similarity in weather patterns. Removing the largest fire event from the training period is a good test of whether events can be detected that are – after removing them – unprecedented in the training period. For these tests, we use the false alarm rate (Wilks, 2011) for skill assessments (a value of 0.0 is perfect and a value of 1.0 denotes no skill).

3 Results

3.1 Extreme Fire Weather Types

Daily time series of burned areas are characterized by a clear seasonal cycle with summer and autumn maxima (Jin et al., 2015) and feature distinct peak events such as shown on the example of the Los Angeles (LA) region in Fig. 1b. Extreme fire days dominate the statistics of total burned area with the top one percent of days accounting between 35 % [±6 %] in the Northern region and 77 % [±18 %] in the San Diego region (shown is the median and standard deviating of the VIIRS, MODIS, and GWIS datasets). The rapid increase and decay of daily burned areas indicates that extreme fire days are closely related to short-term weather conditions more so than slowly changing factors, as found in other regions (Abatzoglou & Kolden, 2011; Riley et al., 2013).

Fig. 2a,b shows the the two identified XWT patterns in the LA region. Using the 10 largest fire days and considering mixing ratio 2 m above ground, sea level pressure, and 10 m wind speed anomaly patterns result in the highest classification skill in this region. The first XWT pattern (LA-A) is associated with intense and very dry Santa Ana winds that arise due to a strong pressure gradient between the U.S. desert Southwest and California (Fig. 2a) (Raphael, 2003). Extreme fires that are associated with this pattern occur most frequently between September and May but can occasionally also happen in late spring, which is in line with previous studies of Santa Ana wind events (Raphael, 2003). The largest daily burned area in the LA region associated with this XWT is the

Old Fire from October 26, 2003 (Fig. 2c). The strong offshore winds resulted in rapid-fire-spread and transported smoke far out into the Pacific.

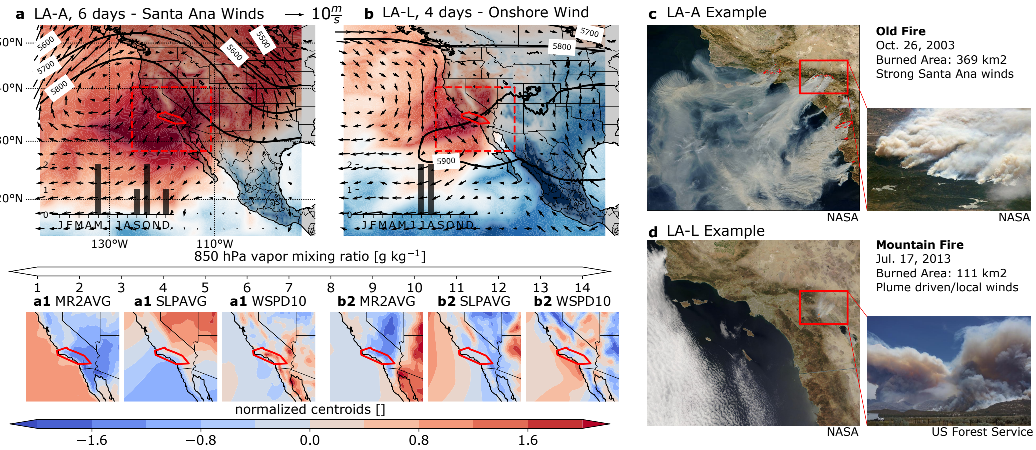

Figure 2. The most extreme fire days are related to archetypal large-scale weather patterns (XWTs). a,b) In the LA region, two XWTs are identified as being related to extreme daily burned areas. The first XWT is associated with strong Santa Anna winds (LA-A) that occur on the west side of a mid-level trough causing very strong and dry offshore winds. The second XWT (b) is related to plume-driven fires that develop under low-pressure anomalies (i.e., thermal low pressure systems; LA-L) in the intermountain West causing onshore advection of moisture at mid-levels. Histograms in the bottom left of a) and b) show the monthly occurance frequency of the XWT days. The centroids of the three variables that characterize the XWTs are shown in (a1, b1). These variables are 2 m above ground mixing ratio (MR2AVG), sea level pressure (SLP), and 10 m wind speed. c,d) Show typical examples of fires under LA-A (wind-driven) and LA-L (plume-driven) conditions.

The second XWT pattern (LA-L) is associated with much weaker large-scale forcing. A thermal low creates almost the opposite pressure distribution as during LA-A with anomalously high pressure over the Pacific and low pressure over the Intermountain West (Fig. 2b) resulting in onshore winds. Fires during LA-L days are typically plume driven and occur most frequently during the hottest months of the year (July and August) (Fig. 2b). A representative example of type LA-L is the Mountain Fire on July 17, 2013 (Fig. 2d).

The XWTs for the other sub-regions are shown in Fig. S2–S8 and summarized in Fig. 3d. The coastal regions – San Diego, LA, Central Coast, and Bay area – each have a strong offshore XWT associated with Santa Ana and Diablo Winds. Additionally, they also feature an XWT that is associated with cyclonic flow due to a thermal low-pressure system leading to onshore flow. The Central Coast has an additional third XWT that is associated with very weak large-scale forcing (CC-W) and results in fires that are largely plume-driven. Atmospheric ridging/troughing causes favorable fire weather conditions in the remaining regions particularly in the Northern region where XWTs are related to troughts in the west (N-TW), east (N-TE), and riding (N-R). Circulation patterns associated with thermal low-pressure systems and anticyclones are important in the Sierra West and Sierra East region. A more detailed description of the XWTs can be found in the supplement.

To better understand the robustness and predictive skill of these XWTs, we perform a leave-one-year-out cross-validation by removing the years with the top four days

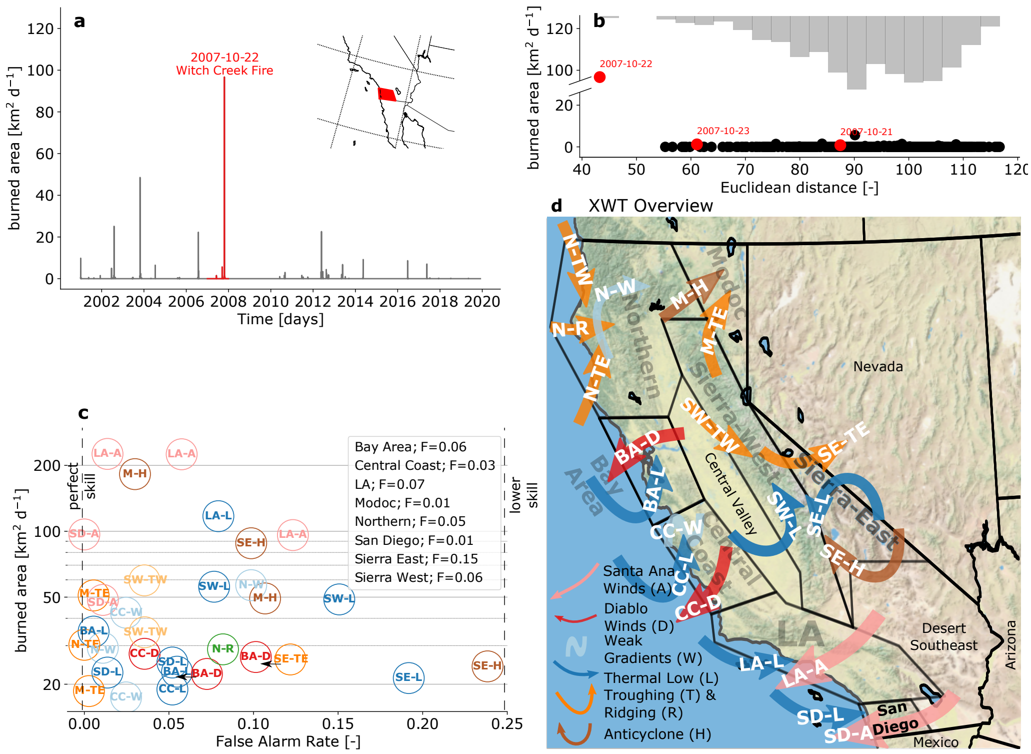

Figure 3. a) Daily burned are time series in San Diego with the Witch Creek Fire fire year highlighted in red. b) Withholding this year from training, the XWT algorithm identifies the Witch Creek fire day (Oct. 10, 2007) as the day with the most favorable burned area conditions (i.e., a small Euclidean distance to identified XWTs) besides being unprecedented in its magnitude in the training period. c) Similar to b) but for the largest four fire days in each region. False alarm rates (FAR) close to zero mean that the fire weather on the withheld extreme fire day was similar to XWTs in the training period. The symbol and font colors show the dominant weather process within the XWT day as described in the legend in d). The average FAR in each region is shown in the legend of c). d) Overview of the synoptic conditions (arrow colors) and predominant low-level wind direction of identified XWTs in all eight sub-regions.

with the largest burned areas each from the training period and test if we can detect the removed extreme day based on the derived XWTs. An example of this test is shown in Fig. 3a for the San Diego region where we removed the year 2007 from the XWT training period, which contained the record-shattering fire growth day of October 22nd (i.e., the Witch Creek fire). The XWTs that are derived by using the remaining years allow us to skillfully detect October 22nd as the most "dangerous" fire weather day of the year according to its large-scale weather conditions (i.e., lowest Euclidean distance to identified XWTs; Fig. 3b). These conditions had a rapid onset and decay since October 21st and 23rd were much less similar to historic XWT conditions and featured much smaller burned areas. This example highlights that the XWT framework can detect extreme events that are unprecedented in the training period as long as the extreme day is related to a synoptic weather pattern that caused large burned areas in the training period. We repeated this analysis for the top four fire days in all sub-regions and calculated the false alarm rate for evaluating the skill of detecting the omitted events (Fig. 3c). Most events can be skillfully detected with the highest skill (lowest false alarm rate) for fires in the

Modoc, the Northern region, San Diego, the Sierra West, and Central Coast region. Lowest skills are fond for the Sierra East region. We also see a tendency that fires with large daily burned areas have lower false alarm rates compared to less extreme fires days. It is important to mention that these skill estimates are conservative since we remove important data points from an already short record.

3.2 Historic Changes in California Fire Weather

To understand long-term historic changes in fire weather frequency, we identify XWT days in the 80-member NOAA-CIRES-DOE 20th Century Reanalysis (NCD20C) (Slivinski et al., 2019), the 40-member Community Earth System Model (CESM) Large Ensemble (LENS) (Kay et al., 2015), and the CESM single forcing 20-member ensemble (SFE) (Deser et al., 2020). NCD20C allows us to calculate "observed" historic changes in XWT frequencies. LENS provides information on the role of natural variability and forced climate change in the observed frequency changes, and SFE allows us to attribute these changes to greenhouse gasses or aerosol forcing changes.

Our reference climate period is 1920–1960, which is compared to the current period 1975–2015 and a future period 2040–2080. We identify XWT days by regriding the XWT centroids (e.g., Fig. 2a1) to the NCD20C, LENS, and SFE grid and searching for days with similar patterns (i.e., low Euclidean distances, see Fig. S9 and S10 for an example). We select the annual event (i.g., the 116 days with the lowest Euclidean distance in the NCD20C record) and count their frequency in each 40-year long period. Other return periods like the one in three year event lead to similar results (not shown).

An example for the frequency changes in the LA-L XWT pattern is shown in Fig. 4b. The NC20C dataset shows large interdecadal variability with a 40 % higher frequency of LA-L XWT days in the current climate than in the reference period. Part of this increase might be cause by forced climate change since the median frequency change in LENS is 20 % over the same time period. LENS shows a clear decrease in LA-L XWT days towards the end of the 21st century, which gets significant (ensemble interquartile spread excludes zero) around 2050. This frequency decrease does not occur in the no-GHG emission simulations, which means that the decrease can be attributed to increased greenhousegas forcing. The no-AER simulations show an even stronger decrease than the LENS ensemble indicating a small increase in LA-L XWT days due to aerosol forcing changes. XWT frequency time series changes for other regions and XWTs are shown in supplementary Fig. S11.

We find the largest and most significant changes in XWT frequencies due to a northward shift in thermal low pressure systems (Fig. 4a). This class of XWTs are projected to significantly decrease in southern California (San Diego and LA region) with an emergence time of significant changes around 2050 and significantly increases in the Central Coast and particularly in the Sierra-West region. The increasing frequency signal already emerged from climate internal viability around 2000 in the Sierra-West region while time of emergence is around 2030 in the Central Coast region according to the LENS dataset. The decrease in southern regions and increase in central regions can both be attributed to increasing greenhousegas emissions (Fig. 4d) and indicate a northward shift in thermal low pressure systems due to atropogenic climate change.

Other XWT frequency changes are less systematic and non-significant (Fig. 4c). Exceptions are the high pressure (M-H) and the trough in the east (M-TE) type in the Modoc region that both significantly decrease in frequency due to increased greenhouse-gas forcing. Historic changes in XWT frequencies can be significant but are largely due to climate internal variability as can be seen in the low correlation between XWT frequency changes in the NCD20C and LENS ensemble (Fig. 4c).

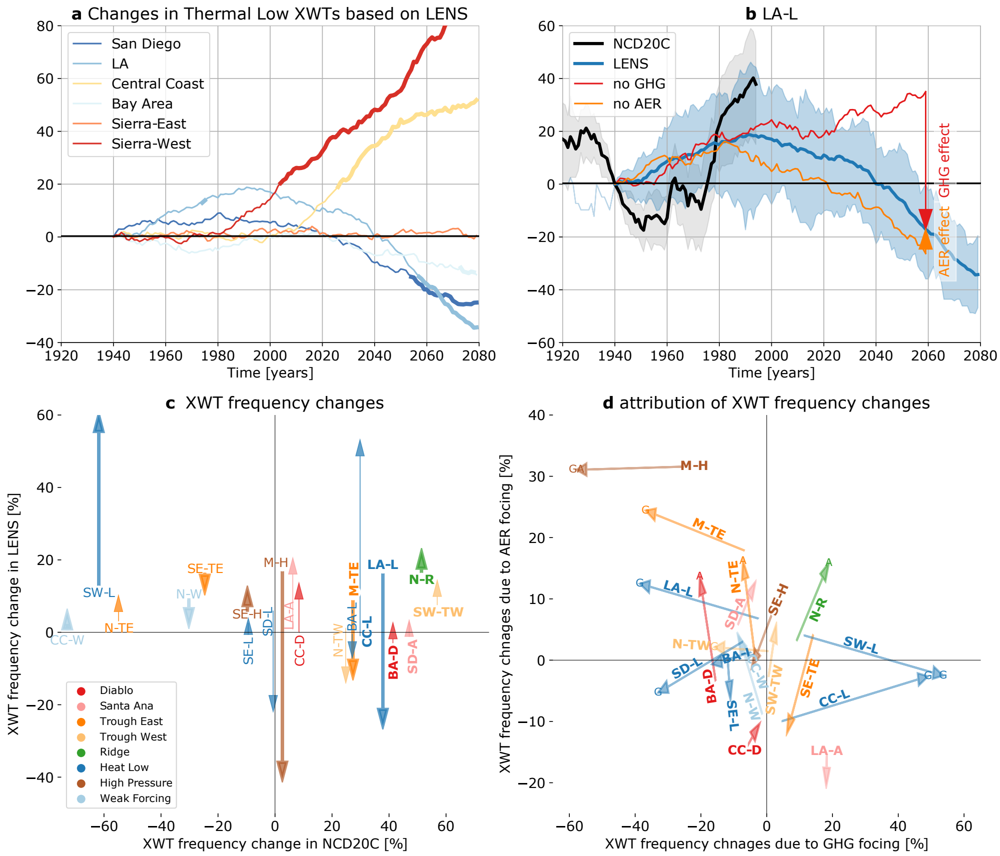

Figure 4. Annual XWT frequency changes during the 20th and 21st century. a) 40-year moving average LENS ensemble median changes in thermal low XWT frequencies in different fire region compared to the reference period (1920–1960). Significant changes (interquantile ensemble spread excludes zero) are shown with bolt lines. b) Frequency changes in the thermal low XWT in the LA region (LA-L) from the NCD20C (black), LENS (blue), no-GHG (red), and no-AER (orange) datasets. The ensemble median is show in bolt lines and the ensemble interquantile spread is shown in blue and gray contours for the LENS and NCD20C data, respectively. c) XWT mean frequency changes in the NCD20C (x-axis) and LENS (y-axis) ensemble for the historic period 1975-2015 minus 1920-1960 (arrow tail) and the LENS projections 2040-2080 minus 1975-2015 (arrows heads). Bold fonts indicate significant change in the NCD20C dataset and thick arrows show significant future changes in LENS. d) Attribution of XWT frequency changes to increasing greenhouse-gas (x-axis) and aerosol concentrations changes (y-axis) based on CESM single forcing runs in the period 1975–2015 (arrow tail) and 2040-2080 (arrow head). Significant changes from greenhouse-gases/aerosols are indicated with a G/A at the arrow head, respectively. Significance is assessed by a two-sided Mann-Whitney U test (P=0.025).

3.3 The Record-Breaking 2020 Fire Season

The 2020 fire season broke several California records. As of December 20, 2020, an area of more than 5,840 km^2 was burned, which is 65 % more than in 2018, which held the previous record (CALFIRE, 2020). Fires in 2020 were most active in northern California where records in the daily burned area were broken in the Central Coast, Bay Area, Northern, and Sierra West regions (according to FIRMS MODIS observations). Similar to previous years, extreme fire days also largely impacted the total burned area in 2020 with the top 3 days accounting for 41 %, 54 %, 26 %, and 28 % of the total burned area in the Central Coast, Bay Area, Northern, and Sierra West regions, respectively. Since 2020 is not included in the previously used datasets, we here use the FIRMS VIIRS real-time dataset to identify the largest burned area days and ECMWF's IFS analysis data for the XWT analyses.

The Bay Area experienced a massive spread of fires on August 19, 2020 (Fig. 5c). Most of these fires were ignited by dry lightning on August 16 and 17. An anticyclone developed off the coast of California on August 18 that intensified and brought strong and dry northeasterly winds to large parts of the Bay Area and Central Coast (Fig. 5a) that were aligned with the underlying topography resulting in an eleven-fold increase in pixel area with detected fires (according to VIIRS) from August 18 to August 19 (Fig. 5f). The anticyclone moved further offshore on August 20, resulting in weaker winds and lower daily burned areas. This pattern represents an XWT that is distinctly different (FAR=0.62) from the two previously identified XWTs (Fig. S4). Searching for this new pattern in ERA5 shows that it previously occurred on July 10, 1985, during the "Northern California Lightning Siege" (Supplementary Fig. S12) where it contributed to large daily burned areas from fires that were started by over 25,000 lightning strikes. The XWT also occurred on July 9, 2018, where it did not cause large burned areas probably due to the lower number of active fires in the region. From our analysis, it is unclear if this new XWT is related to dry lightning but it occurs during the summer months where dry lightning is most frequent. The August 19, 2020 weather pattern was also related to record-breaking daily burned areas in the Central Coast and Northern region.

The second big fire event of 2020 in the Bay Area happened on September 28 where strong offshore winds resulted in rapid fire growth (Fig. 5b). The weather pattern is closely related to BA-D conditions (Diablo winds; the false alarm rate is 0.08).

Another region that saw record-breaking daily burned areas in 2020 is the Sierra West region. The daily burned area record for this region shows a more continuous burning behavior with an area of pixels with detected fires of $\sim$270 km^2 per day between August 20 and September 29 (according to FIRMS VIIRS). The two peak fire days in this region that are at least seven days apart occurred on September 9 and September 17, 2020 (Fig. S13). September 9 does not resemble one of the identified XWTs and is associated with a cutoff-low in the southwestern U.S. that produced strong downslope winds in the region. The September 17 event is related to SW-L but the skill of detection would have been fairly low (false alarm rate is 0.16). This highlights the need to continuously update the identified XWTs since a longer training record length will increase the detection of potentially dangerous patterns and will give us a more complete understanding of the large-scale drivers of extreme fires in California.

4 Conclusions

We show that days with extreme daily burned areas in sub-regions of California are related to distinct extreme weather types (XWTs). Some of these XWTs are associated with well-known fire weather conditions such as Santa Ana or Diablo winds, while others are lesser-known since they occur under weaker large-scale forcing and fire growth depends more on local-scale factors and feedbacks between the fire and the atmosphere

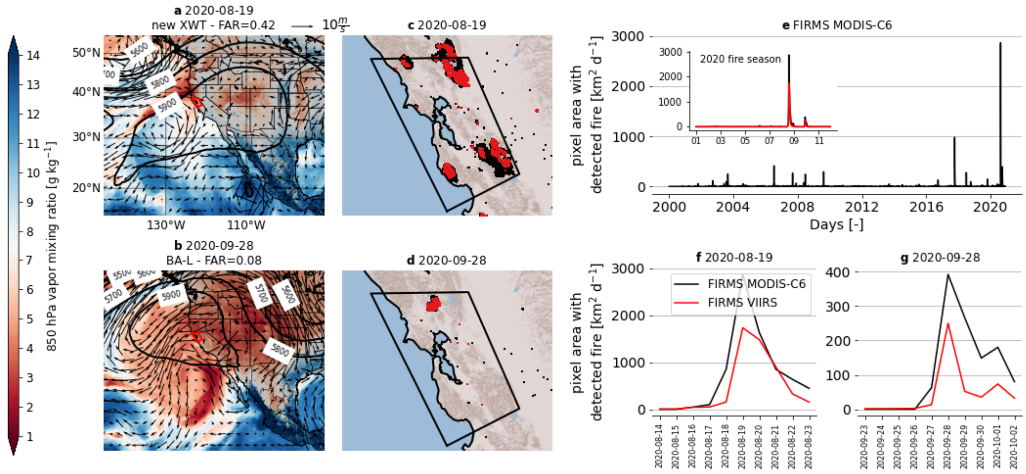

Figure 5. The record-breaking area burned on Aug. 19, 2020, was related to a so-far undetected XWT. (a,b) Large-scale weather pattern during the two days with the largest burned area of 2020 (a, Aug. 19; b, Sep. 28) in the Bay Area, based on IFS model analysis. The titles above the maps show the day, the associated XWT, and the false alarm ratio (FAR). (c,d) Pixels with detected fire for the largest fire day (red) and ±9 days around this day based on VIIRS data (black). (e) Time series of daily pixel area with detected fires in the Bay Area from the FIRMS MODIS-C6 data. (f,g) The period with the August and September peak burned areas from MODIS-C6 (black) and VIIRS (red) data.

(e.g., plume-driven fires). It is important to notice that the occurrence of an XWT day is not sufficient for extreme burned areas since fire ignition and suitable fuels and fuel condition also have to be present. While previous studies have shown a relationship between the occurrence of strong winds (e.g., Santa Ana winds) and fire ignitions from utility lines (Mitchell, 2013) our method did allow us to investigate a correlation between the occurrence of XWTs and dry lightning.

Although some of the XWT frequencies have significantly changed during the 20th century, most of these changes are due to climate internal variability and do not continue into the future. However, future increases in greenhouse-gas concentrations are projected to significantly decrease thermal low XWT frequencies in southern California (San Diego and LA region) and significantly increase their frequencies in the Central Coast and Sierra West region. This indicates a northward shift of thermal lows in the future and will result in a decreased/increased risk of days with large burned areas in the summer months in southern/central California. It is possible that thermal lows XWTs will emerge as a fire XWT in northern California in the future, while they did not dominate fire growth in these regions in the last 20-years. These changes in XWT frequencies will occur on top of other factors such as hotter and drier summers (Lenihan et al., 2003) and future fire activity in California will depend of the interaction of a large variate of climatic and socioeconomic changes.

Our analysis of the 2020 fire season shows that some of the record-breaking fire days were related to weather conditions that were undiscovered using observational records from earlier periods. The combination of a widespread vapor pressure deficit and uncommonly wide-spread dry lightning events in mid-August followed by extremely rare and strong northwesterly winds from an offshore anti-cyclone exemplifies the complex interaction and compounding effects that are related to record-breaking daily burned areas.

This highlights the need for, but also the complexity of, future research to address current and future wildfire risks in California and other fire hotspots around the world. Important fire XWTs might be missing from this analysis due to the short period for which intradaily satellite active fire detection data exists. Extending the daily burned area record and continuously updating the here-defined XWTs is, therefore, important.

Acknowledgments

NCAR is sponsored by the National Science Foundation. Computer resources were provided by the Computational and Information Systems Laboratory (NCAR Community Computing; `http://n2t.net/ark:/85065/d7wd3xhc`) This work was sponsored in part by the California Energy Commission – Energy Program Investment Charge (EPIC) program under Grant #EPC-18-026. We thank Sean A. Parks for sharing his daily burned area product. ERA5 (Hersbach et al., 2020) data can be accessed from `https://climate.copernicus.eu/climate-reanalysis`. The NOAA-CIRES-DOE 20th Century Reanalysis V3 (Slivinski et al., 2019) data can be downloade from `https://www.psl.noaa.gov/data/20thC_Rean/`. Fire observations can be accessed as follows: The Global Wildfire Information System (GWIS) (Artés et al., 2017) `https://doi.pangaea.de/10.1594/PANGAEA.895835`; Monitoring Trends in Burn Severity (MTBS) (Eidenshink et al., 2007) `https://www.mtbs.gov/direct-download`; Parks (Parks, 2014) by contacting Sean F. S. Parks `sean.parks@usda.gov`; Fire Information for Resource Management System (FIRMS) (Davies et al., 2019) `https://firms.modaps.eosdis.nasa.gov/`. The code for the statistical analysis and visualization of data in this document can be accessed under `https://github.com/AndreasPrein/California_extreme-fire-weather-types.git` (Prein, 2021)

References

Abatzoglou, J. T., & Kolden, C. A. (2011). Relative importance of weather and climate on wildfire growth in interior Alaska. *International Journal of Wildland Fire*, *20*(4), 479–486.

Abatzoglou, J. T., & Williams, A. P. (2016). Impact of anthropogenic climate change on wildfire across western US forests. *Proceedings of the National Academy of Sciences*, *113*(42), 11770–11775.

Amiro, B. D., Logan, K. A., Wotton, B. M., Flannigan, M. D., Todd, J. B., Stocks, B., & Martell, D. (2005). Fire weather index system components for large fires in the Canadian boreal forest. *International Journal of Wildland Fire*, *13*(4), 391–400.

Artés, T., Cencerrado, A., Cortés, A., & Margalef, T. (2017). Time aware genetic algorithm for forest fire propagation prediction: exploiting multi-core platforms. *Concurrency and Computation: Practice and Experience*, *29*(9), e3837.

Artés, T., Oom, D., De Rigo, D., Durrant, T. H., Maianti, P., Libertà, G., & San-Miguel-Ayanz, J. (2019). A global wildfire dataset for the analysis of fire regimes and fire behaviour. *Scientific data*, *6*(1), 1–11.

Balch, J. K., Bradley, B. A., Abatzoglou, J. T., Nagy, R. C., Fusco, E. J., & Mahood, A. L. (2017). Human-started wildfires expand the fire niche across the United States. *Proceedings of the National Academy of Sciences*, *114*(11), 2946–2951.

Bedsworth, L., Cayan, D., Franco, G., Fisher, L., Ziaja, S., & Ackerly, D. D. (2018). *Statewide Summary Report, Californiaâs Fourth Climate Change Assessment.* Governor's Office of Planning and Research. Retrieved from `http://climateassessment.ca.gov`

CALFIRE. (2020). *Incidents overview.* Retrieved from `https://www.fire.ca.gov/incidents/`

Clark, J., Abatzoglou, J. T., Nauslar, N. J., & Smith, A. (2020). Verification of Red Flag Warnings across the Northwestern US as Forecasts of Large Fire

Occurrence. *Fire*, *3*(4), 60.
Davies, D., Ederer, G., Olsina, O., Wong, M., Cechini, M., & Boller, R. (2019). NASA's Fire Information for Resource Management System (FIRMS): Near Real-Time Global Fire Monitoring Using Data from MODIS and VIIRS.
Deser, C., Phillips, A. S., Simpson, I. R., Rosenbloom, N., Coleman, D., Lehner, F., ... Stevenson, S. (2020). Isolating the evolving contributions of anthropogenic aerosols and greenhouse gases: A new CESM1 large ensemble community resource. *Journal of climate*, *33*(18), 7835–7858.
Eidenshink, J., Schwind, B., Brewer, K., Zhu, Z.-L., Quayle, B., & Howard, S. (2007). A project for monitoring trends in burn severity. *Fire ecology*, *3*(1), 3–21.
FIRE, C. (2020). *Top 20 largest california wildfires.* Retrieved from `https://www.fire.ca.gov/media/11416/top20_acres.pdf`
Fosberg, M. A. (1978). Weather in wildland fire management: the fire weather index. *In âProceedings of the Conference on Sierra Nevada Meteorologyâ, 19â21 June 1978, Lake Tahoe, CA. pp. 1â4. (American Meteorological Society: Boston, MA).*
Giglio, L., Boschetti, L., Roy, D. P., Humber, M. L., & Justice, C. O. (2018). The Collection 6 MODIS burned area mapping algorithm and product. *Remote Sensing of Environment*, *217*, 72–85.
Goodrick, S. L. (2002). Modification of the Fosberg fire weather index to include drought. *International Journal of Wildland Fire*, *11*(4), 205–211.
Gregory, D., Morcrette, J.-J., Jakob, C., Beljaars, A., & Stockdale, T. (2000). Revision of convection, radiation and cloud schemes in the ECMWF Integrated Forecasting System. *Quarterly Journal of the Royal Meteorological Society*, *126*(566), 1685–1710.
Haines, D. A. (1989). A lower atmosphere severity index for wildlife fires. *National Weather Digest*, *13*, 23–27.
Hammer, R. B., Radeloff, V. C., Fried, J. S., & Stewart, S. I. (2007). Wildland–urban interface housing growth during the 1990s in California, Oregon, and Washington. *International Journal of Wildland Fire*, *16*(3), 255–265.
Hersbach, H., Bell, B., Berrisford, P., Hirahara, S., Horányi, A., Muñoz-Sabater, J., ... others (2020). The ERA5 global reanalysis. *Quarterly Journal of the Royal Meteorological Society*, *146*(730), 1999–2049.
Hull, M. K., O'Dell, C. A., & Schroeder, M. J. (1966). *CRITICAL FIRE WEATHER PATTERNS, THEIR FREQUENCY AND LEVELS OF FIRE DANGER* (Tech. Rep.). PACIFIC SOUTHWEST FOREST AND RANGE EXPERIMENT STATION BERKELEY CA.
Jin, Y., Goulden, M. L., Faivre, N., Veraverbeke, S., Sun, F., Hall, A., ... Randerson, J. T. (2015). Identification of two distinct fire regimes in Southern California: implications for economic impact and future change. *Environmental Research Letters*, *10*(9), 094005.
Jin, Y., Randerson, J. T., Faivre, N., Capps, S., Hall, A., & Goulden, M. L. (2014). Contrasting controls on wildland fires in Southern California during periods with and without Santa Ana winds. *Journal of Geophysical Research: Biogeosciences*, *119*(3), 432–450.
Jolly, W. M., Cochrane, M. A., Freeborn, P. H., Holden, Z. A., Brown, T. J., Williamson, G. J., & Bowman, D. M. (2015). Climate-induced variations in global wildfire danger from 1979 to 2013. *Nature communications*, *6*(1), 1–11.
Kay, J. E., Deser, C., Phillips, A., Mai, A., Hannay, C., Strand, G., ... others (2015). The Community Earth System Model (CESM) large ensemble project: A community resource for studying climate change in the presence of internal climate variability. *Bulletin of the American Meteorological Society*, *96*(8), 1333–1349.

Lenihan, J. M., Drapek, R., Bachelet, D., & Neilson, R. P. (2003). Climate change effects on vegetation distribution, carbon, and fire in California. *Ecological Applications*, *13*(6), 1667–1681.

McInnes, L., Healy, J., & Astels, S. (2017). hdbscan: Hierarchical density based clustering. *Journal of Open Source Software*, *2*(11), 205.

Mitchell, J. W. (2013). Power line failures and catastrophic wildfires under extreme weather conditions. *Engineering Failure Analysis*, *35*, 726–735.

Parks, S. A. (2014). Mapping day-of-burning with coarse-resolution satellite fire-detection data. *International Journal of Wildland Fire*, *23*(2), 215–223.

Parks, S. A., Miller, C., Parisien, M.-A., Holsinger, L. M., Dobrowski, S. Z., & Abatzoglou, J. (2015). Wildland fire deficit and surplus in the western United States, 1984–2012. *Ecosphere*, *6*(12), 1–13.

Peterson, D. A., Hyer, E. J., Campbell, J. R., Fromm, M. D., Hair, J. W., Butler, C. F., & Fenn, M. A. (2015). The 2013 Rim Fire: Implications for predicting extreme fire spread, pyroconvection, and smoke emissions. *Bulletin of the American Meteorological Society*, *96*(2), 229–247.

Prein, A. F. (2021). *California extreme-fire-weather-types.* (Python code used in the data processing and visualization for the paper entitled "The Character and Changing Frequency of Extreme California Fire Weather" by Prein et al, DOI:10.5281/zenodo.4429364)

Prein, A. F., Holland, G. J., Rasmussen, R. M., Clark, M. P., & Tye, M. R. (2016). Running dry: The US Southwest's drift into a drier climate state. *Geophysical Research Letters*, *43*(3), 1272–1279.

Prein, A. F., & Mearns, L. O. (2021). Us extreme precipitation weather types increased in frequency during the 20th century. *Journal of Geophysical Research: Atmospheres*, e2020JD034287.

Radeloff, V. C., Helmers, D. P., Kramer, H. A., Mockrin, M. H., Alexandre, P. M., Bar-Massada, A., ... others (2018). Rapid growth of the US wildland-urban interface raises wildfire risk. *Proceedings of the National Academy of Sciences*, *115*(13), 3314–3319.

Raphael, M. (2003). The Santa Ana winds of California. *Earth Interactions*, *7*(8), 1–13.

Re, M. (2019). *New hazard and risk level for wildfires in california and worldwide.* Retrieved from `https://www.munichre.com/content/dam/munichre/global/content-pieces/documents/Whitepaper\%20wildfires\%20and\%20climate\%20change_2019_04_02.pdf`

Riley, K. L., Abatzoglou, J. T., Grenfell, I. C., Klene, A. E., & Heinsch, F. A. (2013). The relationship of large fire occurrence with drought and fire danger indices in the western USA, 1984–2008: the role of temporal scale. *International Journal of Wildland Fire*, *22*(7), 894–909.

Saito, T., & Rehmsmeier, M. (2015). The precision-recall plot is more informative than the ROC plot when evaluating binary classifiers on imbalanced datasets. *PloS one*, *10*(3).

Slivinski, L. C., Compo, G. P., Whitaker, J. S., Sardeshmukh, P. D., Giese, B. S., McColl, C., ... others (2019). Towards a more reliable historical reanalysis: Improvements for version 3 of the Twentieth Century Reanalysis system. *Quarterly Journal of the Royal Meteorological Society*, *145*(724), 2876–2908.

Smith, C., Hatchett, B. J., & Kaplan, M. (2018). A surface observation based climatology of Diablo-like winds in Californiaâs wine country and western Sierra Nevada. *Fire*, *1*(2), 25.

Srock, A. F., Charney, J. J., Potter, B. E., & Goodrick, S. L. (2018). The hot-dry-windy index: A new fire weather index. *Atmosphere*, *9*(7), 279.

Tempel, D. J., Gutierrez, R. J., Whitmore, S. A., Reetz, M. J., Stoelting, R. E., Berigan, W. J., ... Peery, M. Z. (2014). Effects of forest management on california spotted owls: implications for reducing wildfire risk in fire-prone forests.

Ecological Applications, *24*(8), 2089–2106.

Thompson, M. P., & Calkin, D. E. (2011). Uncertainty and risk in wildland fire management: a review. *Journal of environmental management*, *92*(8), 1895–1909.

Verisk. (2020). *Wildfire risk analysis.* Retrieved from `https://www.verisk.com/insurance/campaigns/location-fireline-state-risk-report/`

Westerling, A. L. (2016). Increasing western US forest wildfire activity: sensitivity to changes in the timing of spring. *Philosophical Transactions of the Royal Society B: Biological Sciences*, *371*(1696), 20150178.

Wilks, D. S. (2011). *Statistical methods in the atmospheric sciences* (Vol. 100). Academic press.

Williams, A. P., Abatzoglou, J. T., Gershunov, A., Guzman-Morales, J., Bishop, D. A., Balch, J. K., & Lettenmaier, D. P. (2019). Observed impacts of anthropogenic climate change on wildfire in California. *Earth's Future*, *7*(8), 892–910.

Supporting Information for "The Character and Changing Frequency of Extreme California Fire Weather"

Andreas F Prein[1] *, and Janice Coen[1,2], and Abby Jaye[1]

[1]National Center for Atmospheric Research (NCAR), Boulder, CO, USA

[2]University of San Francisco, San Francisco, CA, USA

Contents of this file

1. Figures S1 to S13

Corresponding author: Andreas F. Prein, National Center for Atmospheric Research, Boulder, CA, USA. (prein@ucar.edu)

*3090 Center Green Dr., Boulder, CO
80301, USA

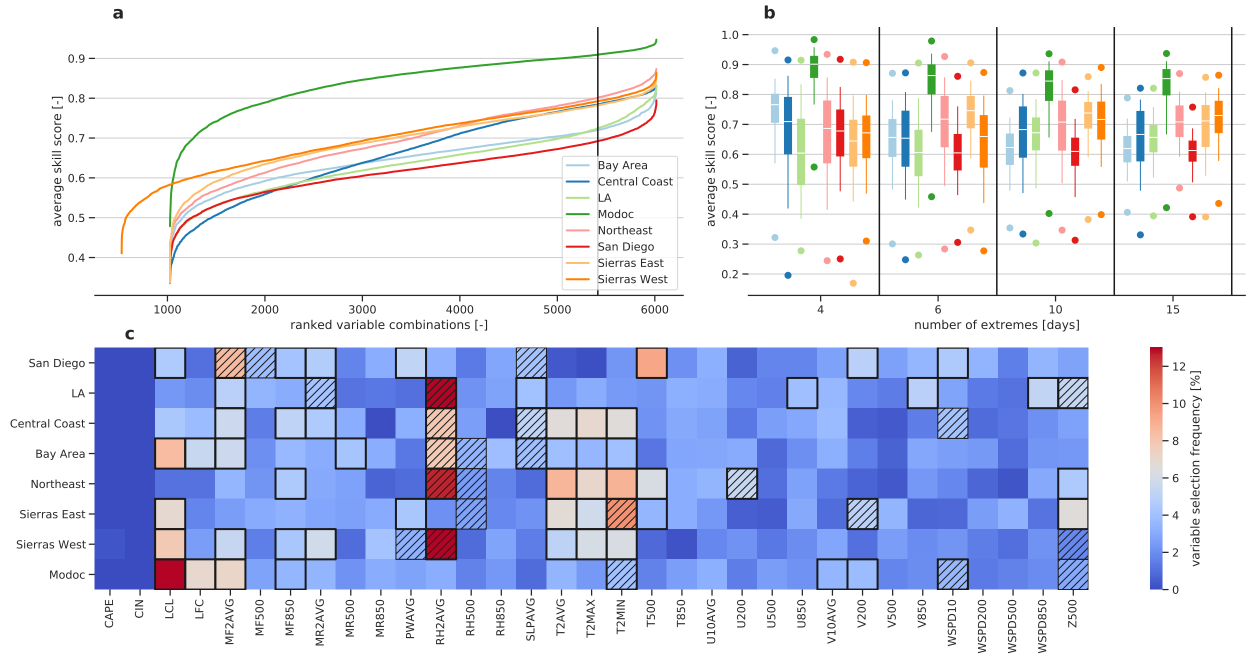

Figure S1: Optimization of the XWT in each of the 8 fire regions. a) Tested variable combination ranked according to their average split sample skill score (zero is perfect). The vertical line shows the 10th percentile of the best performing combinations. b) Box-whisker plots show the skill score spread according to the variable uncertainty. c) Probability frequency heatmap showing how often a variable was picked in the top 10 percent of the best performing variable combinations. The 8 variables that were selected most frequently in the top performing settings are highlighted in black boxes. These are the variables that were used in the testing shown in panel b. The variables that were used in the final XWT are hatched. The tested variables are (from left to right) convective available potential energy (CAPE), convective inhibition (CIN), lifting condensation level (LCL), level of free convection (LFC), moisture flux at 2 m (MF2AVG), 500 hPa (MF500), and 850 hPa (MF850), vapor mixing ratio 2 m (MR2AVG), 500 hPa (MR500), and 850 hPa (MR850), precipitable water (PWAVG), relative humidity at 2 m (RH2AVG), 500 hPa (RH500), and 850 hPa (RH850), sea level pressure (SLPAVG), 2 m average (T2AVG), maximum (T2MAX), and minimum (T2MIN) temperature, mean temperature at 500 hPa (T500), and 850 hPa (T850), zonal wind at 10 m (U10AVG), 200, hPa (U200), 500 hPa (U500), and 850 hPa (U850), meridional wind at 10 m (V10AVG), 200, hPa (V200), 500 hPa (V500), and 850 hPa (V850), wind speed at 10 m (WSPD10), 200, hPa (WSPD200), 500 hPa (WSPD500), and 850 hPa (WSPD850), and geopotential height at 500 hPa (Z500).

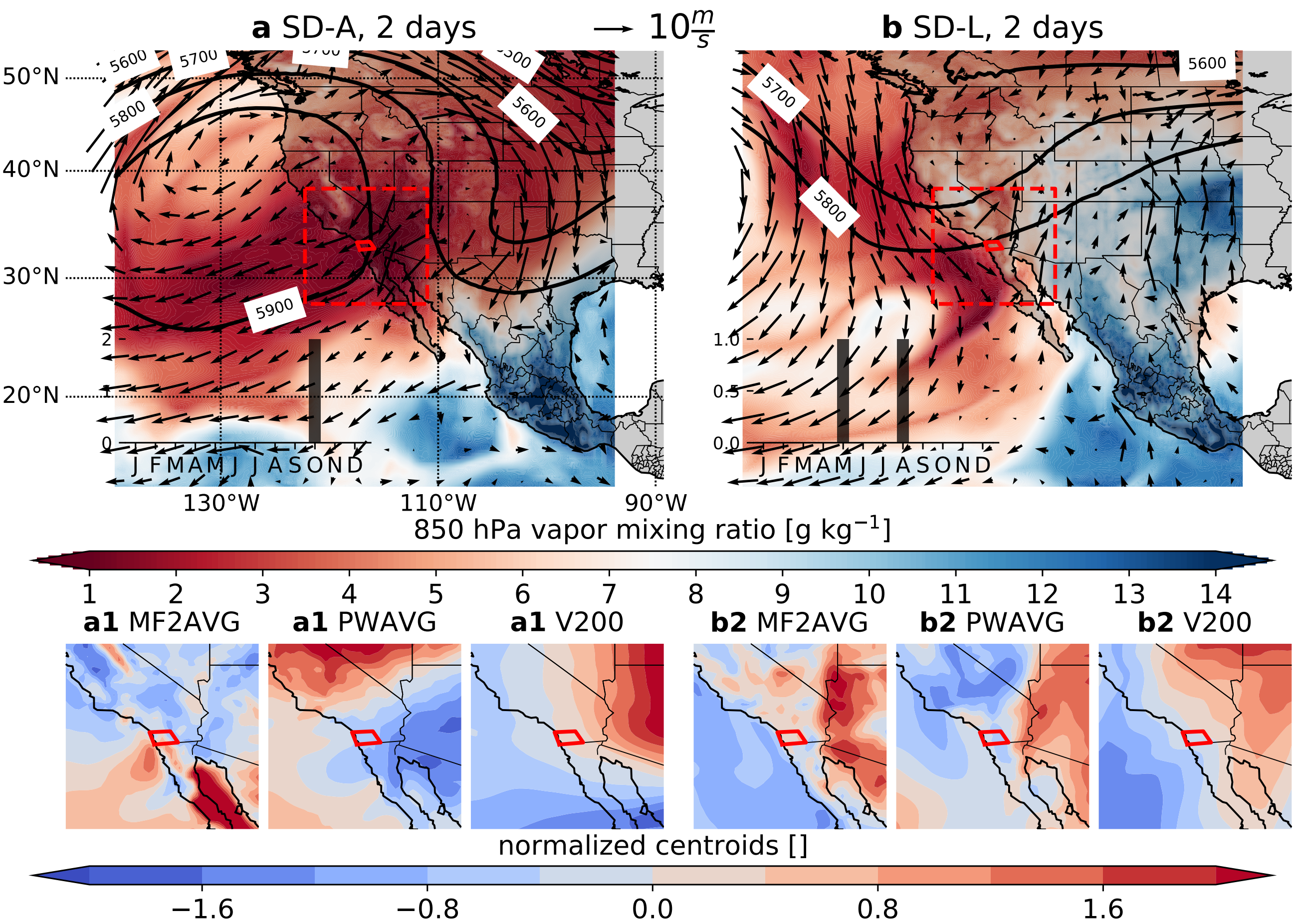

Figure S2: a,b) Two XWTs are identified in the San Diego region. SD-A is associated with strong Santa Ana winds that occur on the west-side of a mid-level trough causing very strong, dry offshore winds. SD-L is related to fires that develop under low-pressure anomalies (thermal lows) in the intermountain West causing onshore advection of moisture at mid-levels. The centroids of the three variables that characterize these XWTs are shown in (a1, b2). These variables are 2 m above ground moisture flux (MF2AVG), daily average precipitable water (PWAVG), and 200 hPa nothward wind speed.

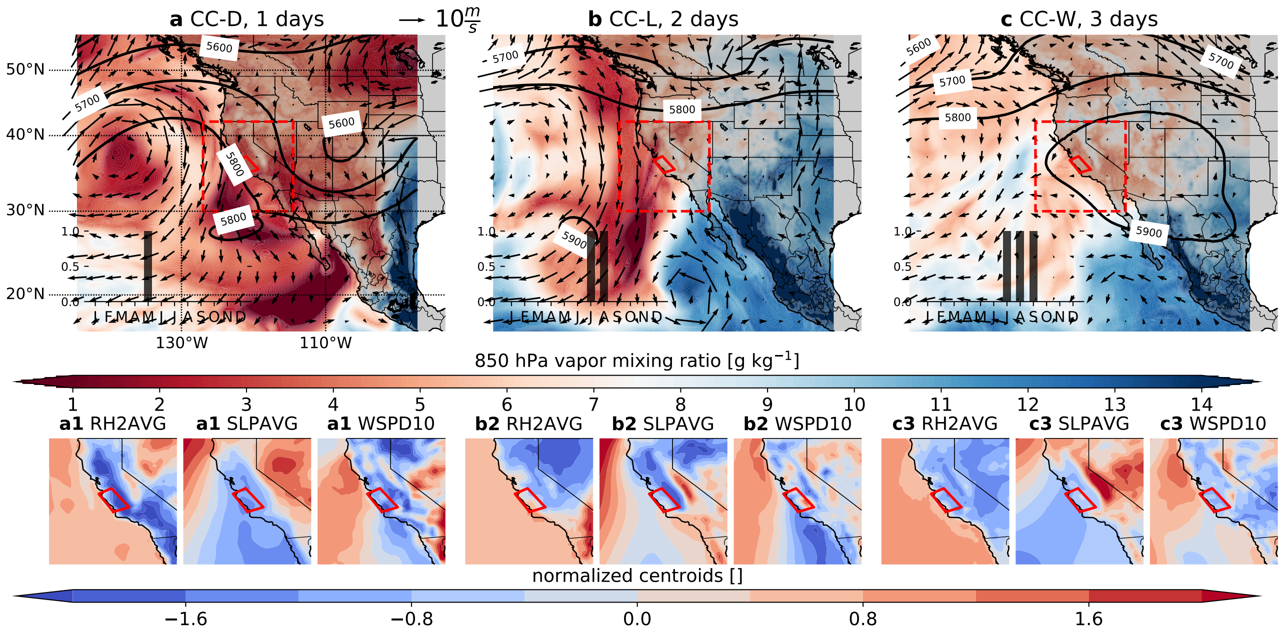

Figure S3: Similar to Supplementary Fig. S2 but showing the 3 identified XWTs in the Central Coast region. CC-D is associated with strong ridging in the west and Diablo Winds along the coast, CC-L features a thermal low and onshore wind advection, and CC-W is associated with weak large-scale forcing and is likely dominated by local scale processes. The XWT centroids are defined by daily average 2 m relative humidity (RH2AVG), sea level pressure (SLPAVG), and 10 m above ground wind speed (WSPD10).

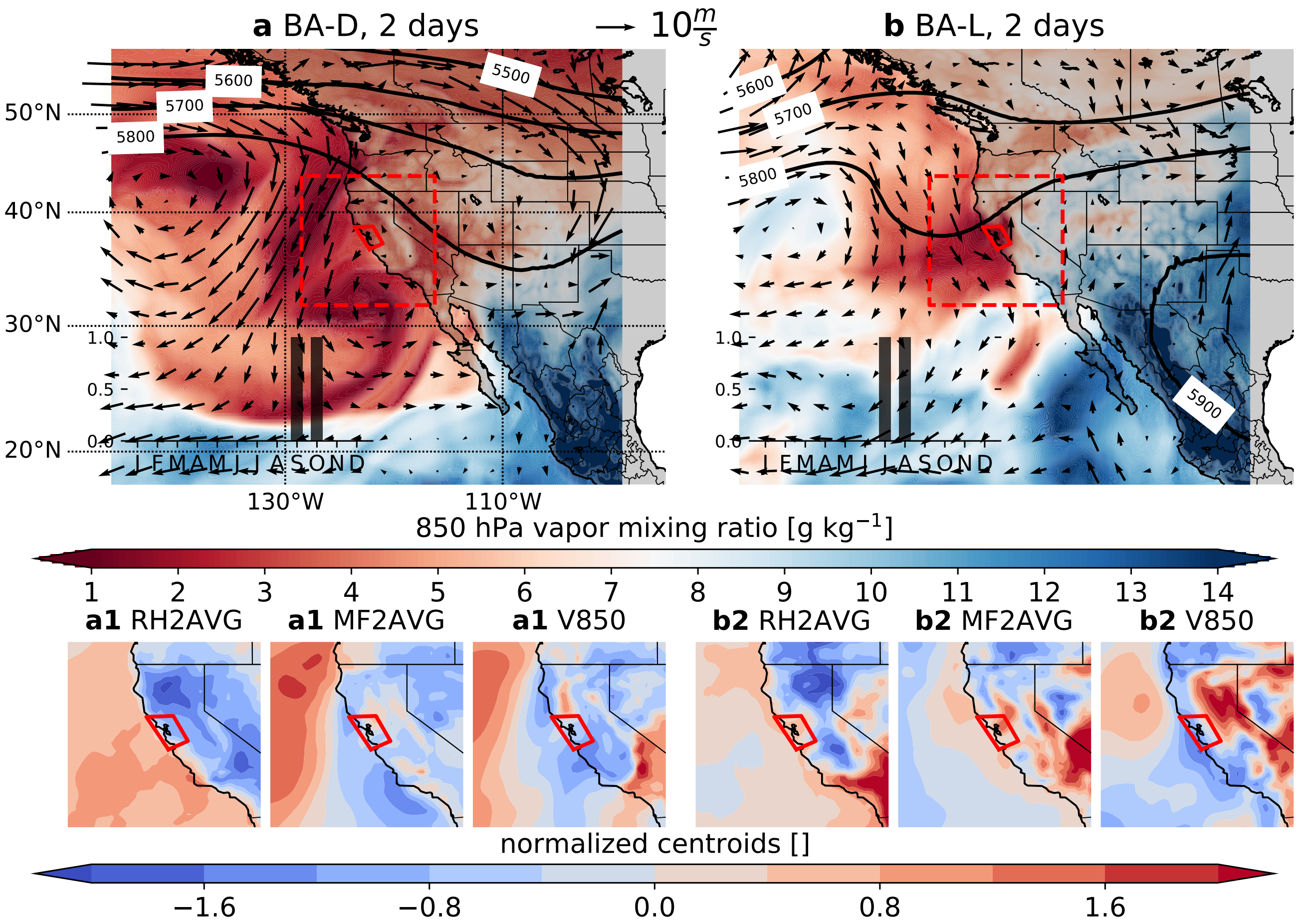

Figure S4: Similar to Supplementary Fig. S2 but showing the 2 identified XWTs in the Bay Area. BA-D is associated with strong offshore, Diablo winds, BA-L features a thermal low and onshore dry wind advection. The XWT centroids are defined by daily average 2 m relative humidity (RH2AVG), 2 above ground moisture flux (MF2AVG), and 850 hPa northward wind speed (V850).

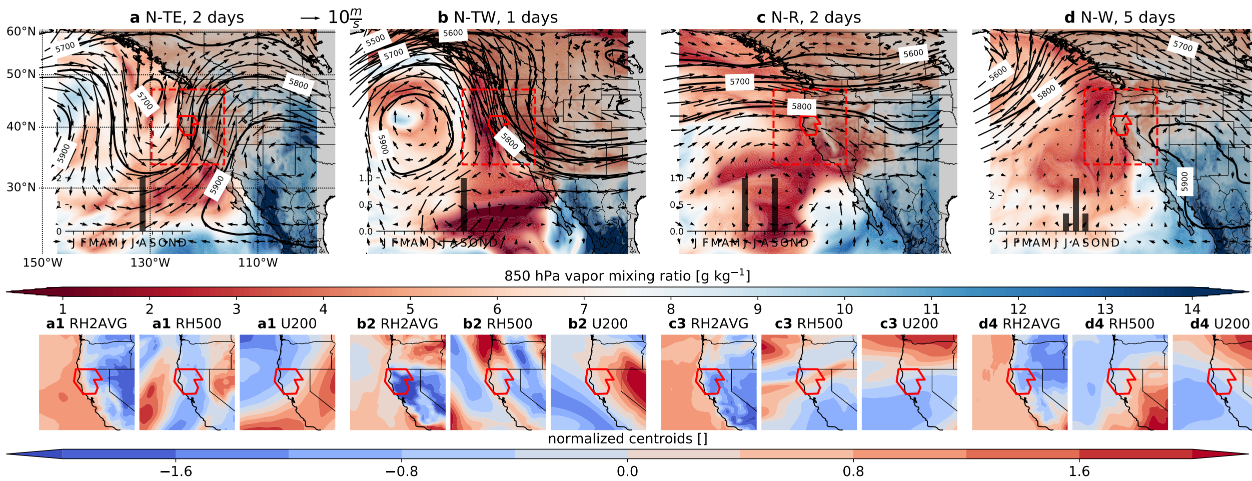

Figure S5: Similar to Supplementary Fig. S2 but showing the four identified XWTs in the Northern region. N-TE is associated with strong south westerly wind advection on the eastern side of a trough, N-TW features strong northerly winds on the western side of a trough, N-R is associated with westerly wind in a ridge, and N-W features northerly wind due to a high pressure ridge over the continent. The XWT centroids are defined by daily average 2 m and 500 hPa relative humidity (RH2AVG), and 200 hPa westward wind speed (U200).

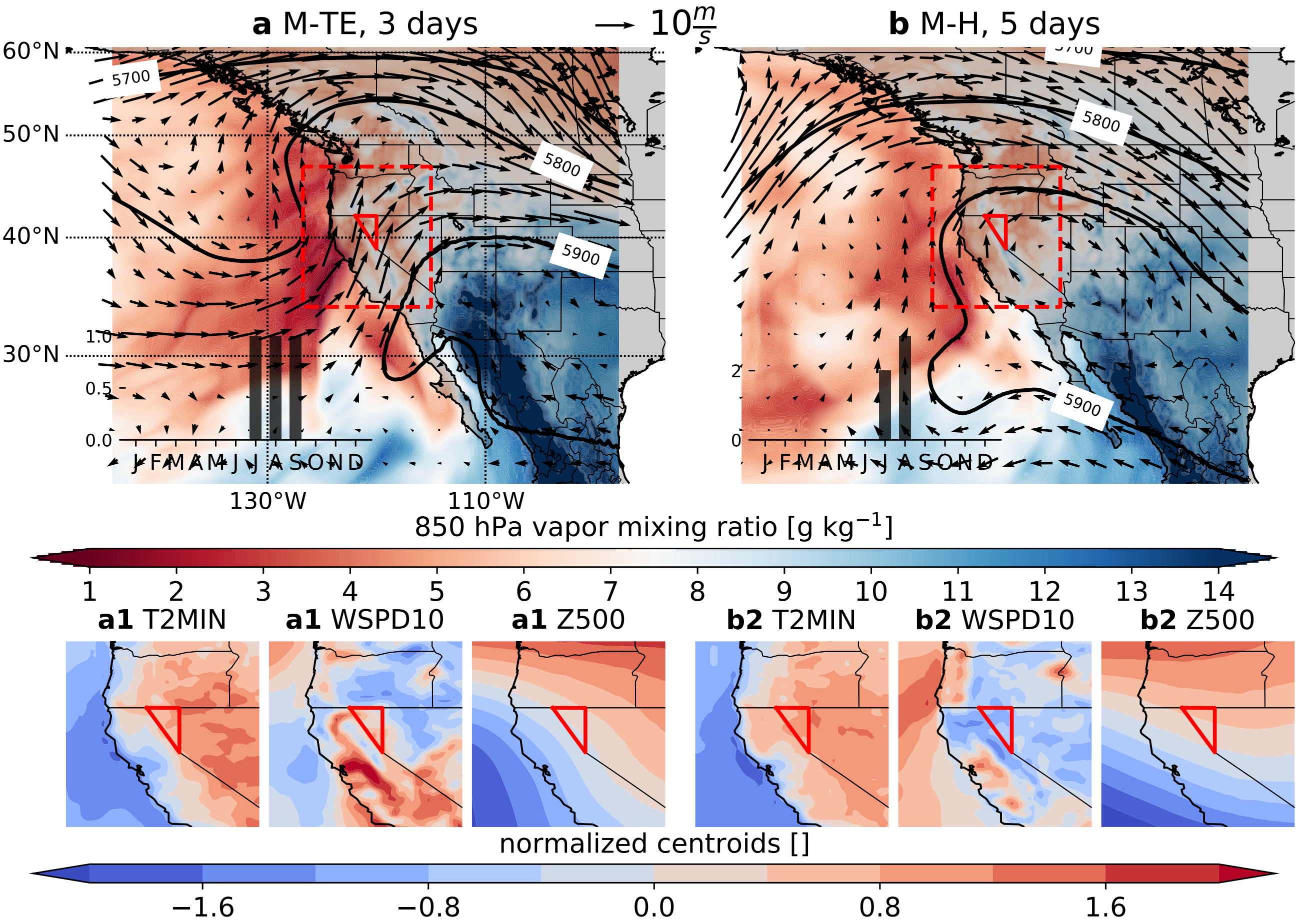

Figure S6: Similar to Supplementary Fig. S2 but showing the two identified XWTs in the Modoc region. M-TE is associated with strong south westerly winds on the eastern side of a trough, and M-H features anticyclonic circulation due to high pressure system over the intermountain west. The XWT centroids are defined by daily minimum 2 m air temperature (T2MIN), 10 m above ground wind speed (WSPD10), and 500 hPa geopotential heights (ZG500).

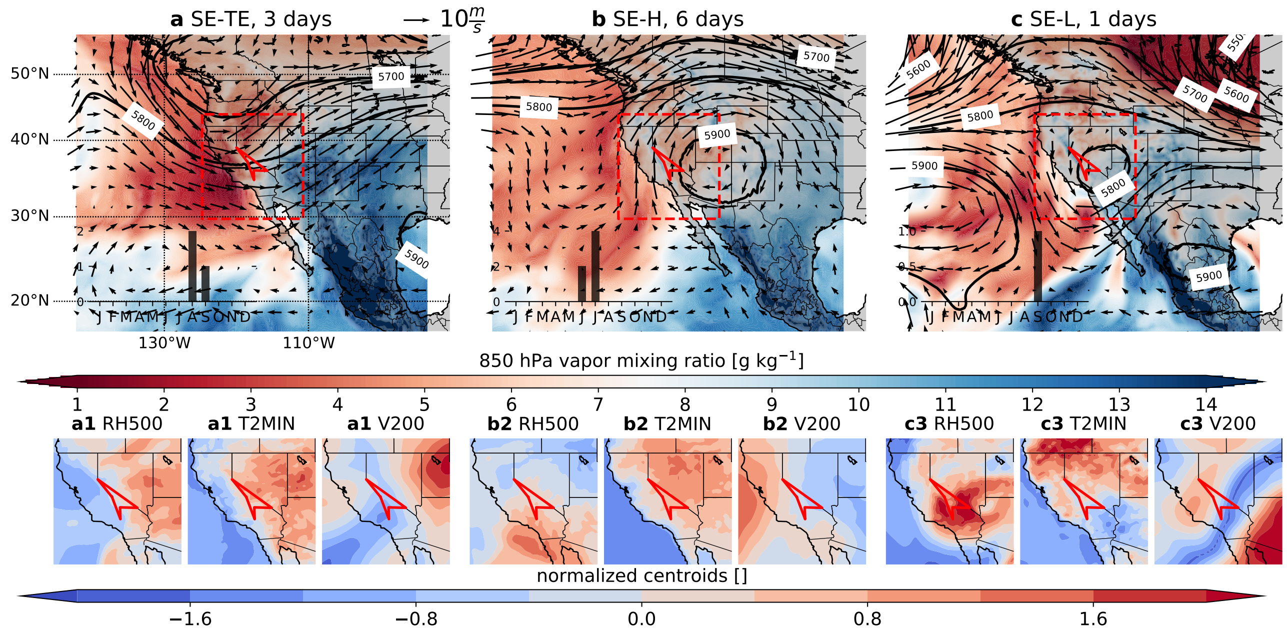

Figure S7: Similar to Supplementary Fig. S2 but showing the three identified XWTs in the Sierra East region. SE-TE is associated with strong westerly winds within a trough, SE-H features strong southerly winds caused by an anti-cyclone over the Four Corners Region, and SE-L is characterized by northerly winds caused by a cutoff low. The XWT centroids are defined by 500 hPa relative humidity (RH500), daily minimum air temperature (T2MIN), and 200 hPa northward wind speed (V200).

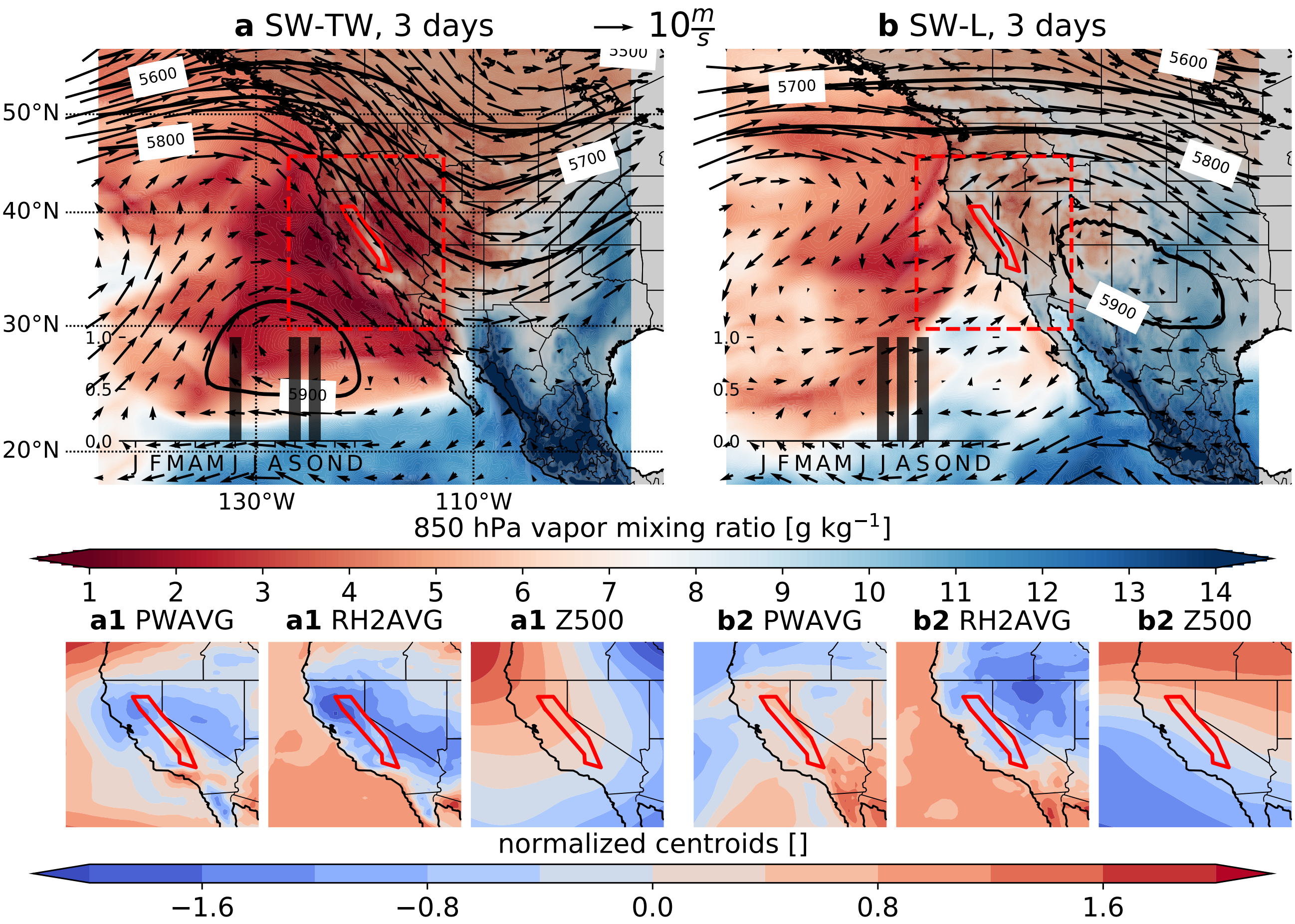

Figure S8: Similar to Supplementary Fig. S2 but showing the two identified XWTs in the Sierra West region. SW-TE is associated with strong northwesterly winds on the west-side of a trough, SW-L is characterized by northeasterly winds within a thermal low pressure system. The XWT centroids are defined by precipitable water (PWAVG), 2 m above gorund relative humidity (RH2AVG), and 500 hPa geopotential height (Z500).

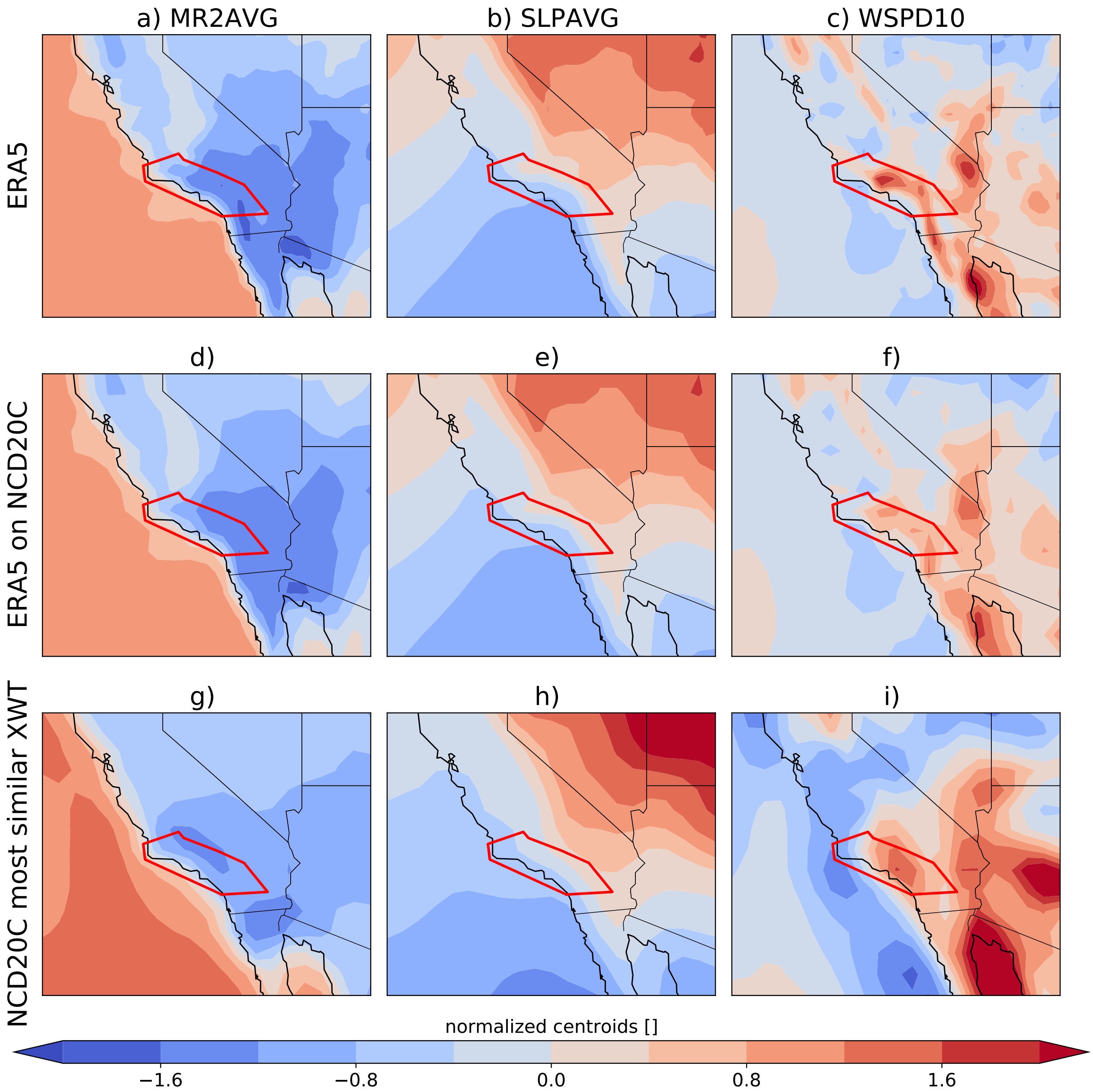

Figure S9: Example for detecting XWTs in the NOAA-CIRES-DOE 20th Century Reanalysis (NCD20C). The original LA-A XWT centroids (a–c) are regrided to the NCD20C grid (d–f). Euclidean distances are calculated between these patterns and all days in the NCD20C dataset. The normalized anomaly fields for the day with the lowest Euclidean distance (14.6 on October 20, 1904) is shown in (g–i).

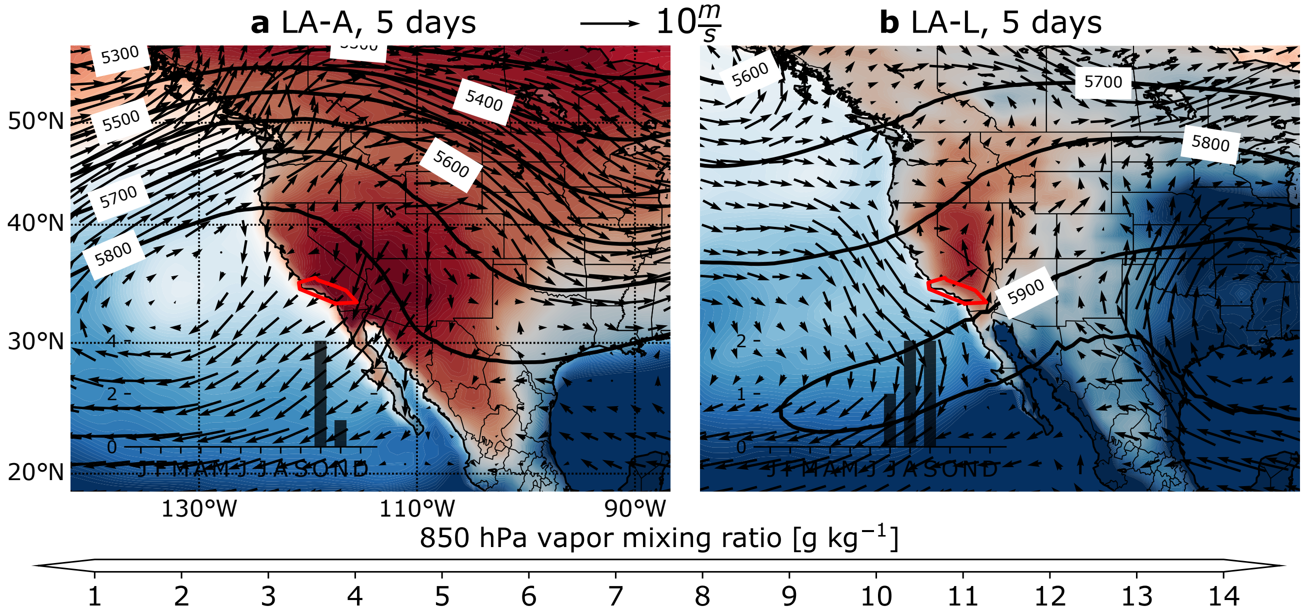

Figure S10: Average synoptic scale conditions for the five most similar days (lowest Euclidean distance) in the NCD20C member-1 compared to LA-A. The map shows the same variables as Fig. 2a,b except for the filled contour which shows Q2 instead Q850 since the latter is not available for NCD20C.

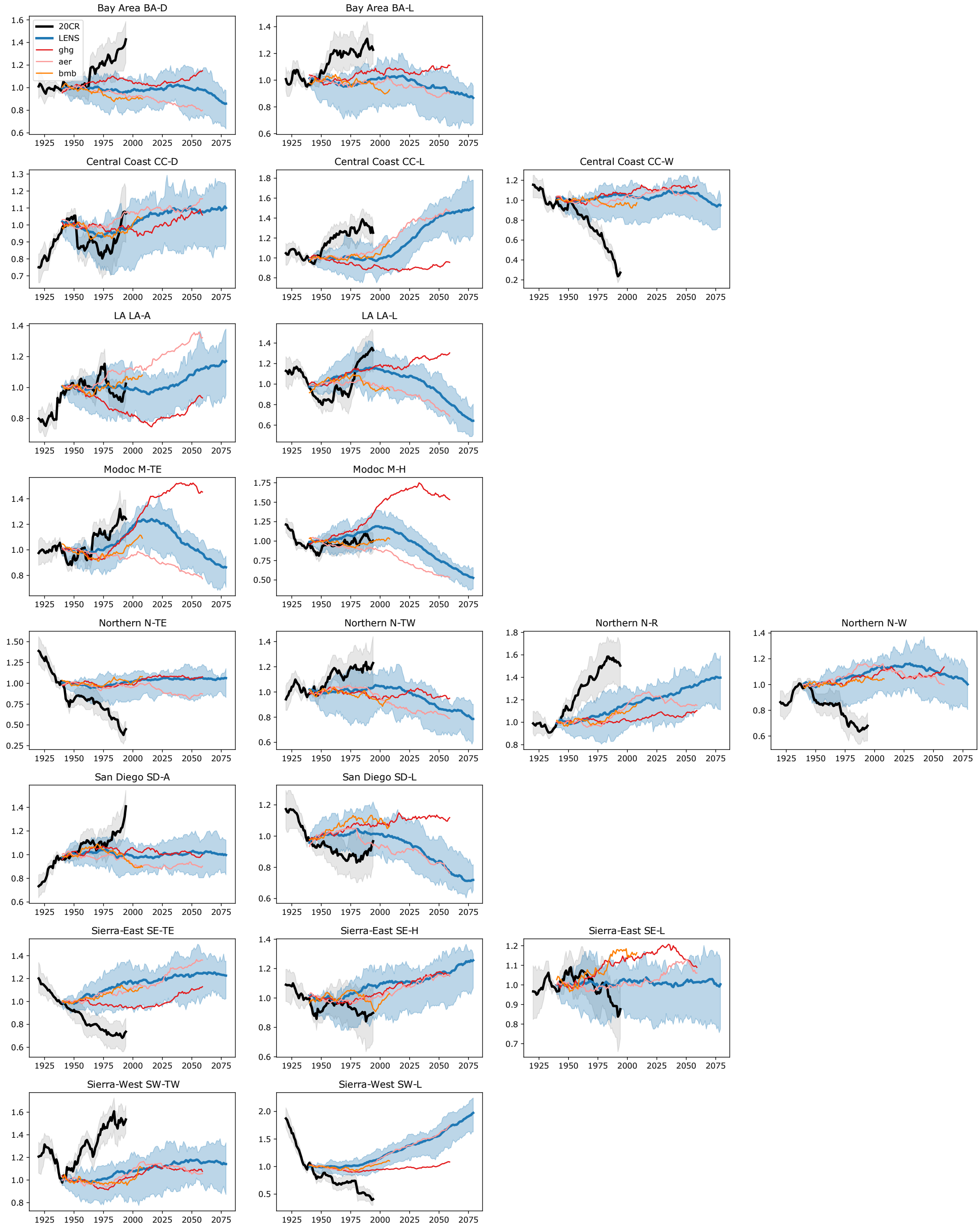

Figure S11: Frequency changes in the annual XWT event relative to the reference period 1975–2015. Shown are time series for each fire region (rows) and XWTs (columns) from the 20CR (black), LENS (blue), simulations without greenhouse gases changes (ghg; red), without aerosols changes (aer; pink), and without landsurface changes (bmb; orange). Thick lines show ensemble median changes. The interquantile ensemble spread is shown for the 20CR and LENS data (contours). All time series are low-pass filtered with a 40-year moving average filter.

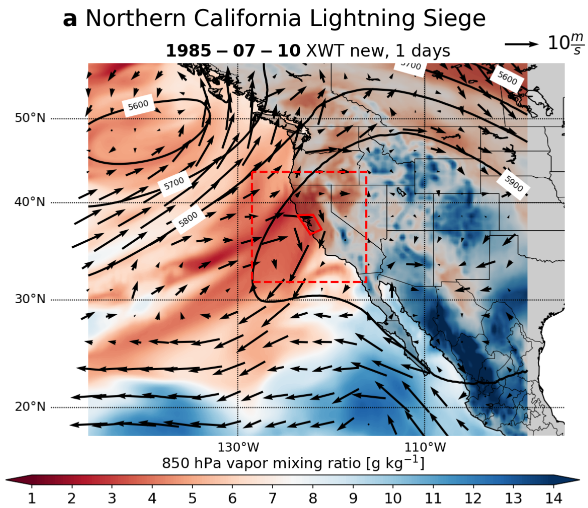

Figure S12: Occurrences of the new Bay Area XWT that was related to the record breaking daily burned area in August 2020. Similar conditions caused large burned areas during the Northern California Lightning Siege of 1985 (a) whereas the same pattern did not cause large burned areas during its occurrence in July 2018 likely due to a smaller number of active fires before its onset.

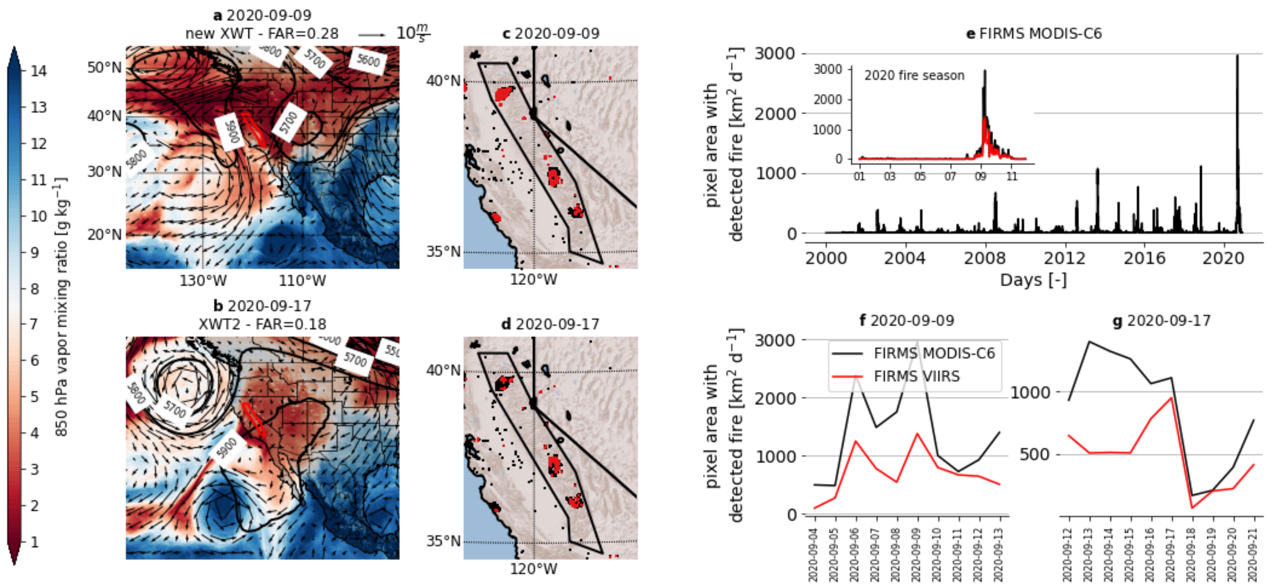

Figure S13: The record-breaking burned area on Aug. 9, 2020, in the Sierra West region was related to a so-far undetected XWT. (a,b) Large-scale weather pattern during the two days with the largest burned area of 2020 in the Sierra West region (a, Aug. 9; b, Aug. 17), based on IFS model analysis. The titles above the maps show the day, the associated XWT, and the false alarm ratio (FAR). (c,d) Pixels with detected fire for the largest fire days (red) and ±9 days around this day based on VIIRS data (black). (e) Time series of daily pixel area with detected fires in the Sierra West region from the FIRMS MODIS-C6 data. (f,g) Zoom into the time period with the two fire outbreaks showing the MODIS-C6 (black) and VIIRS (red) data.